

MoSe₂ Modified ZIF-8 Novel Nanocomposite for Photocatalytic Remediation of Textile Dye and Antibiotics Contaminated Wastewater

Honey Mittal¹, Aruna Ivaturi² and Manika Khanuja^{*1}

¹Centre for Nanoscience and Nanotechnology, Jamia Millia Islamia, New Delhi-110025, India

²Smart Materials Research and Device Technology (SMaRDT) Group, Department of Pure and Applied Chemistry, University of Strathclyde, Glasgow G1 1XL, UK

**Corresponding author: manikakhanuja@gmail.com*

Abstract

COVID-19-led antibiotic waste generated from hospitals and health centers may cause serious health issues and significantly impact the environment. In the coming decades, antibiotic resistance will be one of the most significant threats to global human health. Photocatalytic water remediation is an effective and promising environmental solution that can be utilized to address this issue to convert antibiotic waste into non-toxic products by utilizing renewable and abundant solar energy. In the present study, a novel nanocomposite of Zeolitic imidazolate frameworks (ZIF-8) and molybdenum diselenide (MoSe₂) were efficiently synthesized by the solvothermal method for the complete degradation of the antibiotics and textile waste from water. The morphology, crystallinity and band gap of the samples were characterized by field emission scanning electron microscopy (SEM), X-ray diffraction (XRD) and UV-Visible Spectroscopy. Fourier transform infrared spectroscopy (FTIR) and X-ray photoelectron spectroscopy (XPS) provides the binding information of the sample. The photocatalytic activity was tested for degradation of the antibiotics: Tetracycline Hydrochloride (TC) and Metronidazole (MNZ)) used in COVID-19 treatment and textile dye: malachite green. Time-resolved photoluminescence spectroscopy confirmed the enhanced charge separation in MoSe₂@ZIF-8 nanocomposite with an average lifetime of 4.72 ns as compared to pristine samples. The nanocomposite showed ~100% removal efficiency with rate constant of 63×10^{-3} , 49×10^{-3} and $42 \times 10^{-3} \text{ min}^{-1}$ for TC, MNZ and Malachite green, respectively. The photocatalytic degradation of TC was carried out under different pH conditions (4, 7 and 9) and the degradation mechanism was explained on the basis of Zeta potential measurements and active species trapping experiment. The byproducts of the photocatalytic treatment of TC antibiotics were tested using Liquid Chromatography-Mass Spectroscopy (LC-MS) and they were found to be non-toxic for aquatic and human life. The regeneration property of the nanocomposite was confirmed by FESEM with regeneration efficiency of 88.7% in the 4th cycle. Thus,

32 MoSe₂@ZIF-8-based photocatalysts have potential application in water remediation, especially in
33 making the antibiotic waste less toxic.

34 **Keywords:** TCSPC, Photocatalysis, Zeta Potential, Antibiotics, COVID-19

35 **1. Introduction**

36 COVID-19 has resulted in an increased pharmaceutical waste in the environment, rivers and
37 coastal waters (Chen et al. 2021) (Dharmaraj et al. 2021). Antibiotic waste management is a critical
38 problem because of its high environmental and human health hazards (Tsai 2021, Wang et al.
39 2020a). Antibiotics are not easily metabolized resulting in the expulsion of their residues through
40 feces and urine to the aquatic ecosystem leading to serious environmental problems (Li et al. 2020).
41 Moreover, these antibiotics cannot be removed by traditional procedures such as biological
42 processes, filtration, coagulation and sedimentation (Adams et al. 2002, Barhoumi et al. 2017,
43 Stackelberg et al. 2007). Tetracycline Hydrochloric (TC) and Metronidazole (MNZ) have been
44 explored as potential therapeutic drugs in treating COVID-19 patients because of their potential
45 antiviral properties (Gharebaghi et al. 2020, Sodhi & Etminan 2020). Tetracycline Hydrochloric
46 antibiotics are primary antibiotic groups found in the different ecosystems that is used for human
47 therapy (viral infections and inflammatory disorders) and agricultural purposes (Daghrir & Drogui
48 2013, Sodhi & Etminan 2020). Recently, a computational study has shown that TC plays a key role
49 in treating SARS-CoV-2 main proteases and COVID-19-related lung disease (Gironi et al. 2020).
50 Metronidazole (MNZ) is the most widely used of the second-generation quinolones and is used to
51 treat joints, gastroenteritis, respiratory tract and cellulitis. MNZ is a redox-active prodrug that acts
52 as a biocidal agent and studies have revealed that it decreases the COVID-19 infection (Gharebaghi
53 et al. 2020). However, MNZ induces an acute and sub-lethal effect on most species of aquatic life.
54 One serious water pollution concern involving the discharge of antibiotic waste into the water
55 bodies is the possibility of the development of antibiotic-resistant bacteria in the wastewater
56 (Dharmaraj et al. 2021). Dyes are primary constituents of textile wastewater and, constitute a group
57 of toxic and carcinogenic contaminants.

58 For the treatment of antibiotic and textile wastewater, photocatalysis is a facile, highly efficient
59 environmental-friendly and straightforward technology as compared to other conventional
60 techniques (Adams et al. 2002, Ashraf et al. 2020, Kumar et al. 2022, Kumar et al. 2020, Mittal et
61 al. 2019, Qin et al. 2021). ZIF-8 has been considered a potential photocatalyst for CO₂ reduction,

62 water-splitting and photocatalytic degradation due to its large surface areas, well-defined porous
63 structures and superior photocatalytic performance (Chin et al. 2018, Li et al. 2019b, Peng et al.
64 2020, Shinde et al. 2021). However, ZIF-8-based photocatalysts are limited due to the low electron
65 discharge ability and high recombination rate of photogenerated electron-hole pairs (Fu & Ren
66 2020, Qiu et al. 2018). Therefore, to overcome the issues related to ZIF-8 and improve its catalytic
67 performance, the nanocomposite of ZIF-8 with MoSe₂ was constructed. Molybdenum diselenide
68 (MoSe₂) has been proven to be a potential co-catalyst for photocatalysis due to more active sites
69 and reduced recombination rate of charge carriers (Mittal & Khanuja 2020a, Siddiqui et al. 2018).
70 Therefore, it is advantageous to construct a nanocomposite by combining the photocatalytic
71 properties of MoSe₂ with the strong adsorbing properties of ZIF-8 to generate a potential
72 photocatalyst to degrade antibiotic wastes.

73 In this study, we have synthesized a novel photocatalyst by a two-step method: The Hydrothermal
74 method for MoSe₂ and the solvothermal method for the synthesis of MoSe₂@ZIF-8
75 nanocomposite. A series of pollutants (antibiotics: TC, MNZ and dye: Malachite green) are used
76 to evaluate the degradation efficiency of the synthesized samples. MoSe₂@ZIF-8 nanocomposite
77 showed enhanced degradation efficiency, ~3 times higher than pristine MoSe₂. The degradation
78 efficiency obtained at different pH (4, 7 and 9) was explained using zeta potential measurements.
79 The highest degradation efficiency for TC was observed in the alkaline medium due to the effect
80 of electrostatic attraction between TC²⁻ and the positive charge on the surface of the
81 nanocomposite. The proposed photocatalysis mechanism was supported by a scavenger
82 experiment that confirms the role of active species in the degradation of pollutants. Repeated
83 experiments confirmed the reusability and regeneration ability of the nanocomposite. To the best
84 of our knowledge, the MoSe₂@ZIF-8 nanocomposite has not been reported before for wastewater
85 treatment.

86 **2. Experimental Section**

87 **2.1. Materials**

88 Sodium molybdate (Na₂MoO₄) with 99.99% purity and hydrochloric acid (HCl.H₂O) with 99.96%
89 purity was bought from Thermo Fisher Scientific India Pvt. Ltd. Selenium (Se, 99.99%) and
90 hydrazine hydrate (N₂H₄.H₂O) with 98% purity was bought from Central Drug House Pvt. Ltd. To

91 prepare ZIF-8, 2-methylimidazole (98%) and zinc nitrate (Zn (NO₃)₂) were obtained from Loba
92 Chemie Pvt. Ltd. Milli-Q water was used for all the experimental work.

93 2.2. Synthesis of MoSe₂@ZIF-8 Nanocomposite

94 For the synthesis of ZIF-8, solution A was prepared by dissolving 0.585 g of zinc nitrate in 4 mL
95 of Milli Q water using a magnetic stirrer. Solution B was prepared by dissolving 2-
96 methylimidazole in 40 mL of Milli Q water followed by the 6 mL of DMSO also known as linker
97 solution. Solution A was then added to the Linker solution and magnetically stirred for 5 min,
98 forming a milky white solution. The obtained solution was centrifuged at 15000 rpm for 15 min
99 followed by washing and drying to yield ZIF-8 (Kaur et al. 2017). MoSe₂ was prepared by the
100 hydrothermal method according to a previously reported study (Mittal &Khanuja 2020a). Fig. 1
101 showed the schematic for the synthesis of MoSe₂@ZIF-8 nanocomposite. MoSe₂@ZIF-8
102 nanocomposite was synthesized using a similar method as ZIF-8. In the above procedure, 0.1g of
103 MoSe₂ was dissolved in 6 mL of DMSO before its addition to the linker solution and magnetically
104 stirred for 5 min. All the further steps were similar to the synthesis of pristine ZIF-8 (Chen et al.
105 2019). Finally, obtained MoSe₂@ZIF-8 material was labeled as ZM.

106

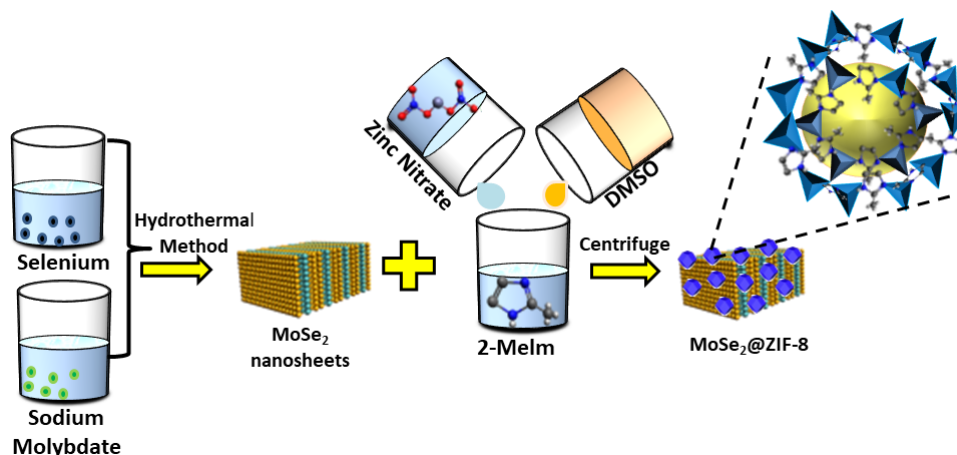
107

108

109

110

111



112

Fig. 1: Synthesis mechanism of MoSe₂@ZIF-8 Nanocomposite

113

2.3. Characterization

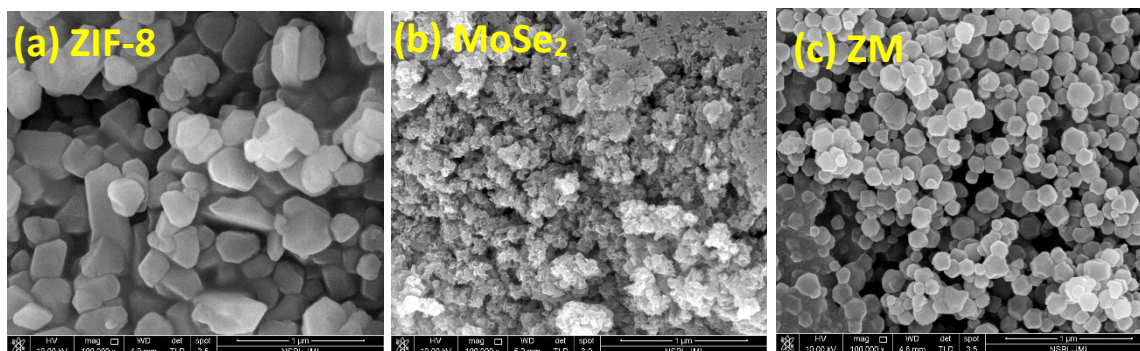
114 The morphology of the prepared samples was characterized using FESEM-Field Emission
115 Scanning Electron Microscope (Quanta 3D FEG). X-ray diffraction (XRD) diffractograms were
116 recorded using Rigaku Smart Lab XRD. Samples were characterized for optical study using a UV-

117 Vis spectrometer (Agilent technologies, Cary 100 series). Thin films of the samples were prepared
118 by dissolving in ethanol for functional groups study and spectra were recorded by Fourier
119 transform infra-red (FTIR) spectroscopy (Bruker Tensor 37 FTIR spectrometer). X-ray
120 photoelectron spectroscopy (XPS) was collected on ESCA+ Omicron Nano Technology with a
121 characteristic energy of 1486.7eV. Surface charge measurement of the samples was performed
122 using Zeta potential (Malvern Zetasizer Nano ZS) using ethanol as dispersing solvent. Time
123 Correlated-Single Photon Counting (TCSPC) measurement of the samples was recorded using a
124 spectrometer (Horiba (DeltaFlex01-DD)). The intermediate and final degraded products of
125 antibiotic degradation solution were examined by Liquid Chromatography-Mass Spectroscopy
126 (LC-MS) from the Xevo TQD system.

127 3. Results and Discussion

128 3.1. Morphology and components

129 Fig. 2 (a-c) shows FESEM micrographs of ZIF-8, MoSe₂ and ZM nanocomposites. It is observable
130 in Fig. 2(a), that pure ZIF-8 nanoparticles are polyhedrons with an average particle size of ~300
131 nm. Fig. 2(b) clearly shows the nanosheets of MoSe₂. As shown in Fig. 2(c), ZM nanocomposites
132 consist of well-shaped polyhedrons of ZIF-8 nanoparticles with an average particle size of about
133 116 nm uniformly dispersed on the surface of MoSe₂ nanosheets.

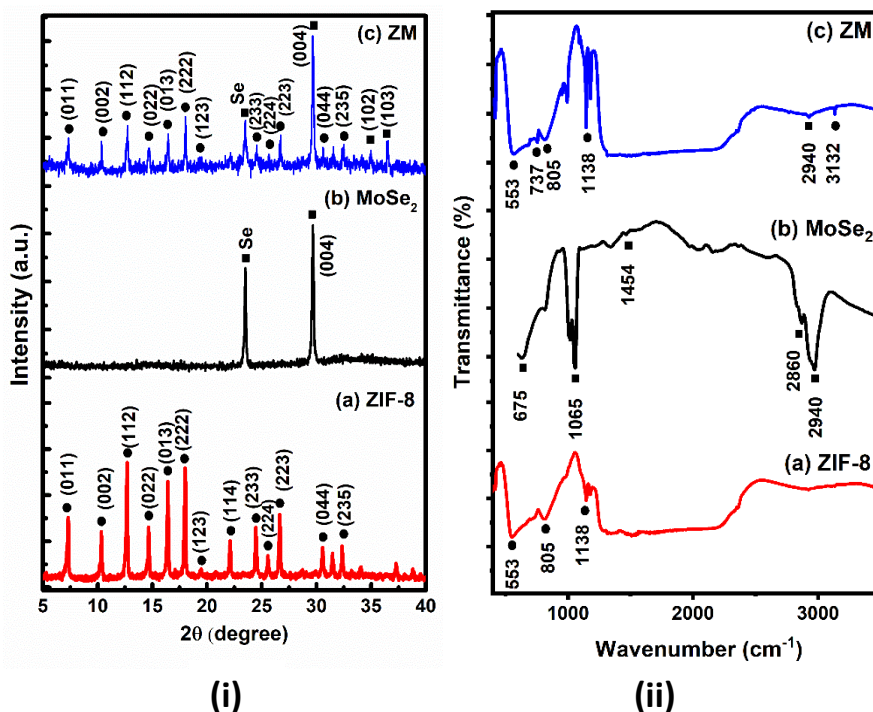


134 **Fig. 2: FESEM images of (a) ZIF-8, (b) MoSe₂ and (c) ZM nanocomposite**

135 The structural properties of MoSe₂, ZIF-8 and the ZM nanocomposite were investigated by XRD
136 [Fig. 3 (a-c)]. The XRD pattern of the pristine ZIF-8 [Fig. 3(a)] showed diffraction peaks at 7.3°,
137 10.3°, 12.7°, 14.7°, 16.4°, 18.0°, 19.3°, 22.1°, 24.6°, 25.6°, 26.7°, 30.6° and 32.3° corresponds to
138 (011), (002), (112), (022), (013), (222), (123), (114) (233), (224), (223), (044) and (235) planes of

139 ZIF-8, respectively (JCPDS Card No: JCPDS 00-062-1030) (Si et al. 2018). In MoSe₂ [Fig. 3(b)],
 140 the main peak at 29.6° corresponds to the (004) plane. Both ZIF-8 and MoSe₂ peaks were observed
 141 in the ZM nanocomposite, which implies that the ZIF-8 is in close contact with the MoSe₂
 142 nanosheets.

143 FTIR spectra of ZIF-8, MoSe₂ and ZM nanocomposite are shown in Fig. 3 ii(a-c). ZIF-8 and ZM
 144 have similar FTIR peaks, indicating that surface modification does not destroy the fundamental
 145 structural framework. In the FTIR spectra of ZIF-8 in Fig. 3 ii(a), the bands at 553 cm⁻¹ and 805
 146 cm⁻¹ are assigned to the out-of-plane bending of 2- methyl imidazole rings (Ulu 2020). The peak
 147 located at 1138 cm⁻¹ is assigned to the C-N vibration of the imidazole ring (Wu et al. 2017). In the
 148 FTIR spectra of MoSe₂ as shown in Fig. 3 ii(b), the peaks located at 1065 cm⁻¹ and 1454 cm⁻¹ are
 149 assigned to Se-O and carboxylate (COO⁻) stretch (Liu et al. 2017). The peaks located at higher
 150 frequencies 2860 cm⁻¹ and 2940 cm⁻¹ are attributed to the presence of acyclic stretching of C-H
 151 (Harpeness et al. 2003, Liu et al. 2017). Compared with the FTIR analysis of pristine ZIF-8, the
 152 ZM nanocomposite [Fig. 3 ii(c)] showed the existence of an adsorption band at 3132 cm⁻¹
 153 corresponding to the methyl group present in the linker and imidazole ring (Kaur et al. 2017).



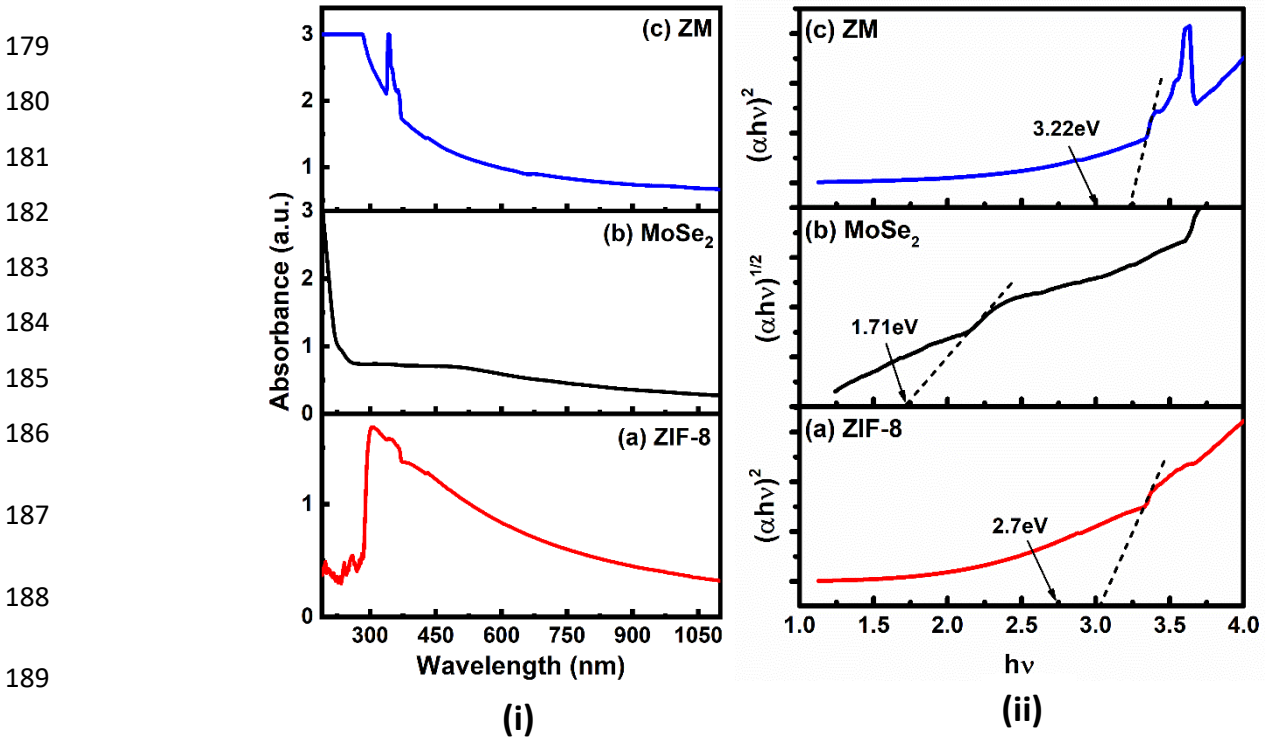
163 **Fig. 3: (i) XRD diffractograms and (ii) FTIR spectra of (a) ZIF-8, (b) MoSe₂ and (c) ZM**
 164 **nanocomposite**

165 UV-Vis absorption spectra of the ZIF-8, MoSe₂ and ZM nanocomposite are shown in figure 4 i(a-
 166 c), respectively. All the samples show absorbance in the wavelength range of 200 to 800 nm. The
 167 ZIF-8 had maximum absorbance at 305 and 350 nm, while the ZM nanocomposite at 340 and 365
 168 nm.

169 The band gap of samples is calculated from the Tauc's plot as shown in Fig. 4 ii(a-c). The energy
 170 band gap values were calculated using Eq. (i):

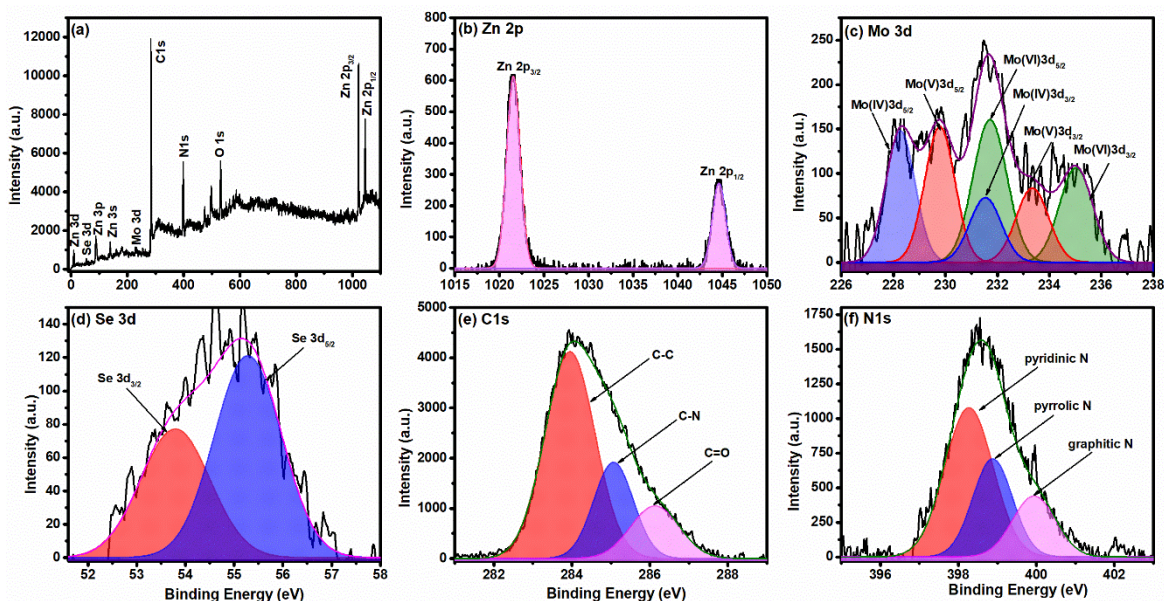
$$171 \quad \alpha h\nu = (h\nu - E_g)^n \quad (i)$$

172 where h is the Planck's constant, α is the absorption coefficient, ν is the frequency, E_g is the
 173 bandgap of the photocatalyst, n is the number that determines the transition property which is taken
 174 as 0.5 for direct bandgap and 2 for indirect bandgap semiconductor (Mittal & Khanuja 2021). In
 175 this case, MoSe₂ is an indirect bandgap semiconductor whereas ZIF-8 is a direct bandgap
 176 semiconductor, however, in the bandgap calculations of ZM nanocomposite, n is taken as 2
 177 because ZIF-8 is the base material (Chen et al. 2019). The MoSe₂, ZIF-8 and ZM nanocomposite
 178 exhibited absorbance in the visible region with the band gap of 1.71 eV, 2.70 eV and 3.22 eV.



191 **Fig. 4: (i) UV absorbance spectra and (ii) Tauc's plot of (a) ZIF-8, (b) MoSe₂ and (c) ZM**
 192 **nanocomposite**

193 XPS spectra were used to investigate the elemental valence and bonding information of the ZM
 194 nanocomposite. The survey spectrum shown in Fig. 5 (a) confirms the presence of Zn, Mo, Se, C,
 195 O and N. The peaks located at 1021.6 eV and 1044.6 eV binding energies in Fig. 5 (b) are assigned
 196 to Zn 2p_{3/2} and Zn 2p_{1/2} of Zn²⁺, respectively (Jia et al. 2018). As seen in Fig. 5 (c), peaks centered
 197 at 229.78 eV and 233.1 eV corresponds to the binding energies of Mo(V)(3d_{5/2}) and Mo(V)(3d_{3/2})
 198 respectively, which indicates the formation of Mo-Se bonds, whereas peaks at 228.27 and 231.54
 199 eV correspond to Mo⁴⁺ characteristics and peaks at 231.72 and 235.03 eV correspond to Mo⁶⁺,
 200 respectively. The XPS results of Se 3d are displayed in Fig. 5 (d), the Se 3d core level demonstrates
 201 two peaks at 53.8 and 55.3 eV that can be attributed to Se 3d_{3/2} and Se 3d_{5/2}, respectively,
 202 representing an oxidation state of -2 for Se in MoSe₂ (Bi et al. 2015, Ge et al. 2018). The high-
 203 resolution N 1s core level spectrum in Fig. 5 (e) can be deconvoluted into three prominent peaks
 204 at 398.3, 398.9 and 399.9 eV, which are attributed to the pyridinic, pyrrolic and graphitic nitrogen,
 205 respectively (Li et al. 2018). As shown in Fig. 5 (f), the C 1s core level spectrum can be
 206 deconvoluted into three peaks centered at 283.9, 285.1, and 286.1 eV, corresponding to C-C, C-N
 207 and C-O bindings, respectively (Luanwuthi et al. 2015). It is observed that the binding energies of
 208 the Zn 2p, Mo 3d and Se 3d peaks in ZM nanocomposite are shifted to lower binding energy by 1
 209 eV, implying that the MoSe₂ and ZIF-8 are interacting with each other (Chen et al. 2019). Thus,
 210 the above detailed material characterizations confirm the successful synthesis of ZM
 211 nanocomposite.



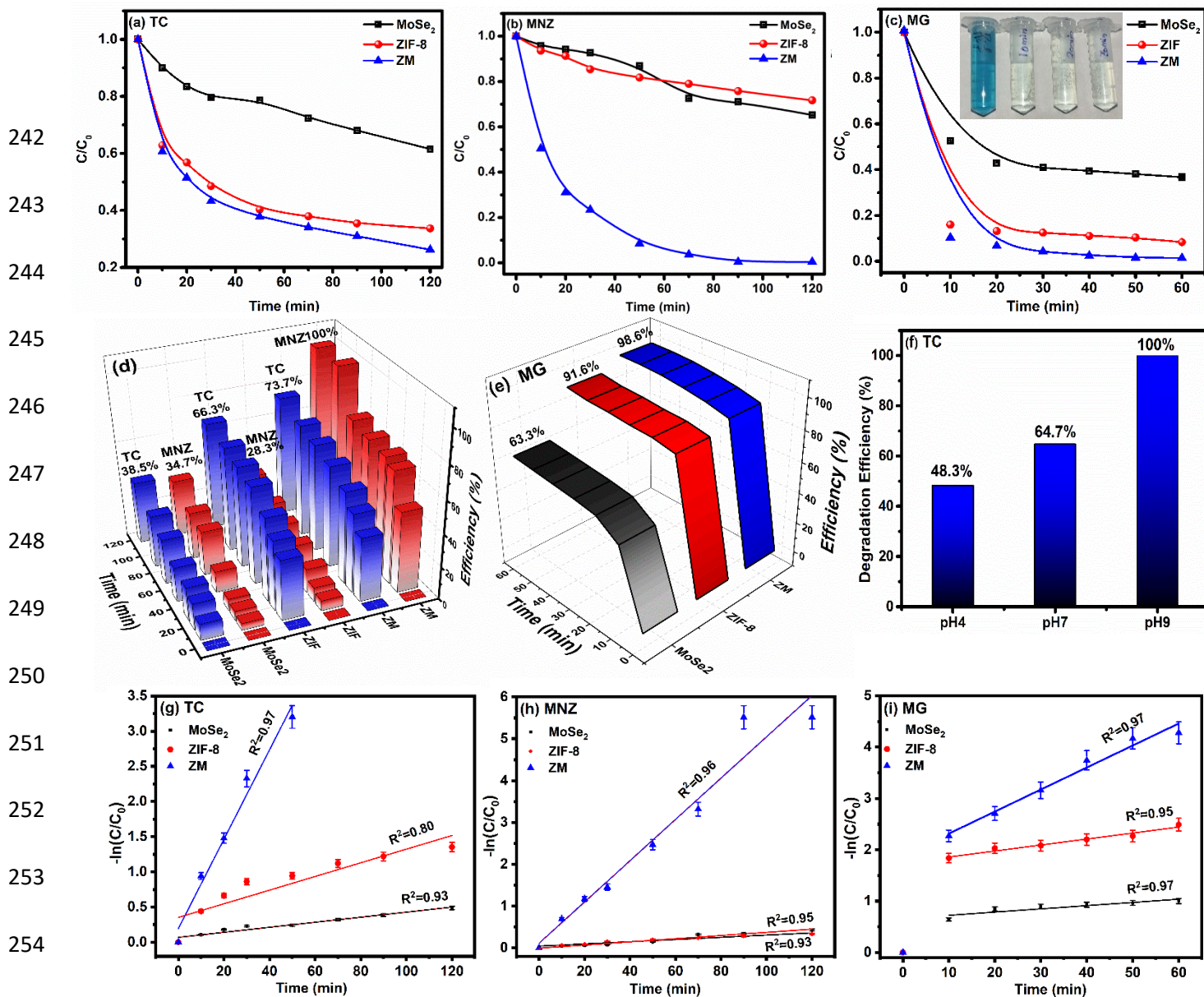
212 **Fig. 5: (a) XPS survey spectra survey of ZM nanocomposite and high-resolution core spectra**
213 **of (b) Zn 2p, (c) Mo 3d, (d) Se 3d, (e) N 1s and (f) C1s**

214 **3.2 Photocatalytic activity**

215 The comparative photocatalytic degradation of Metronidazole (MNZ) and Tetracycline
216 hydrochloride (TC) antibiotics and Malachite Green (MG) dye in aqueous solutions was performed
217 using MoSe₂, ZIF-8 and ZM nanocomposites under light irradiation from Xenon arc lamp (AM
218 1.5G solar illumination 100 mW/cm²). For each photocatalytic degradation test, 20 mg of
219 photocatalyst and 1mg of the target pollutant were used in 100 mL of milli Q water. During light
220 irradiation, 2 mL of the solution was taken out at a fixed interval for UV-Vis spectroscopy. The
221 absorbance peaks for MNZ (318 nm), TC (357 nm) and MG (618 nm) were measured using UV-
222 Visible spectroscopy and a decrease in intensity with irradiation time was measured (Huang et al.
223 2013, Medidi et al. 2018, Saghi &Mahanpoor 2017). The photocatalytic degradation efficiency (η)
224 was calculated using $\eta = \left(1 - \frac{C}{C_0}\right) 100\%$, where, C₀ and C represents degradation of pollutant
225 before and after irradiation at time t, respectively.

226 The degradation and efficiency plots are shown in Fig. 6 (a-e). The photocatalytic degradation
227 efficiency of TC [Fig. 6 (a)] by MoSe₂, ZIF-8 and ZM nanocomposite is 38.5%, 66.3% and 73.7%,
228 respectively. The degradation of MNZ (Fig. 6b) by MoSe₂, ZIF-8 and ZM nanocomposite are
229 34.7%, 28.3% and 99.4%, respectively. The degradation of MG dye by MoSe₂, ZIF-8 and ZM
230 nanocomposite is 63.3%, 91.6% and 99.4%, respectively. Malachite green dye was decolorized,
231 as shown in the inset of Fig. 6(c). As observed from the results, the photocatalytic degradation
232 efficiency of the ZM nanocomposite was enhanced as compared to pristine MoSe₂ and ZIF-8.

233
234
235
236
237
238
239
240
241



256 **Fig. 6: Photocatalytic degradation of MoSe₂, ZIF-8 and ZM nanocomposite, C/C₀ plot for (a)**
 257 **TC (b) MNZ antibiotics and (c) MG dye; efficiency (η) vs time (min) plot for (d) TC, MNZ**
 258 **antibiotic and (e) MG dye; (f) degradation plot of TC under different pH conditions using**
 259 **ZM nanocomposite; First order kinetics plot of (g) TC, (h) MNZ and (i) MG**

260 3.3 Photocatalytic Properties

261 3.3.1 Effect of pH

262 The pH of the solution highly influences the photocatalytic degradation activity because it can
 263 affect both catalyst and pollutant. In this study, the photocatalytic degradation of TC by ZM
 264 nanocomposite was studied under different pH conditions (acidic pH 4, basic pH 9 and neutral pH

265 7) as shown in Fig. 6 (f). When the pH of the solution was 4, 7 and 9, the photocatalytic degradation
 266 efficiency of TC was 48%, 64.7% and 99.4%, respectively. The pH value of the solution affects
 267 not only the surface charge and physical-chemical properties of the pollutant and photocatalyst but
 268 also the generation of hydroxyl radicals. At lower pH, the primarily responsible oxidation species
 269 is photogenerated positive holes, however, at neutral pH or higher pH, it is hydroxyl radicals.
 270 According to the experiment, the pollutant degradation efficiency increases with the increasing pH
 271 of the solution.

272 3.3.2 Rate Kinetics Study

273 To further evaluate the photocatalytic process of the system, the kinetics of photocatalytic activity
 274 was studied using the pseudo-first-order kinetic eq. that was used as follows:

$$275 \quad -\ln\left(\frac{C_t}{C_0}\right) = kt \quad (ii)$$

276 Where, 'k' denotes the rate constant of the reaction.

277 The kinetic studies implies that degradation of TC, MNZ and MG by ZM nanocomposite follows
 278 pseudo-first-order kinetics as shown in figure 6 (g-i) with R² (linear correlation coefficient) value
 279 of 0.97, 0.96 and 0.97, respectively. The k (rate constant) linear correlation coefficient value for
 280 degradation of TC, MNZ and MG by ZM is 0.06 min⁻¹, 0.05 min⁻¹ and 0.04 min⁻¹, respectively.
 281 Rate constant and linear coefficient values for photocatalytic performance of MoSe₂, ZIF-8 and
 282 ZM nanocomposite are summarized in Table 1. The modified surface charge and improved charge
 283 transfer and separation in the ZM nanocomposite makes it more favourable for photocatalytic
 284 activity.

285 **Table 1: Photodegradation efficiency, Rate constant (k) and R² values of prepared**
 286 **photocatalysts**

Pollutant	TC			MNZ			MG		
	MoSe ₂	ZIF-8	ZM	MoSe ₂	ZIF-8	ZM	MoSe ₂	ZIF-8	ZM
Photocatalyst	MoSe ₂	ZIF-8	ZM	MoSe ₂	ZIF-8	ZM	MoSe ₂	ZIF-8	ZM
Efficiency (%)	38.5	66.3	100 (pH 9)	34.7	28.3	100	63.3	91.6	98.6
k x (10 ⁻³) (min ⁻¹)	3.5	9.7	63	2.6	3.8	49	6.2	11	42
R ²	0.80	0.93	0.97	0.93	0.95	0.96	0.97	0.95	0.97

287

288 Till date, several illustrations of semiconductor-MOFs nanocomposites have been reported to
 289 shown potential improvement in the photocatalytic activity, some of them have been listed in Table
 290 2 along with the results of the present study. These findings imply that ZIF-8 and MoSe₂
 291 nanocomposite is a promising photocatalyst for effective degradation of dye and antibiotics.

292 **Table 2: The results of Photocatalytic performance of ZIF-8, MoSe₂ and their**
 293 **nanocomposites reported in literature**

Photocatalyst	Morphology	Pollutant	Efficiency (η)-Light Conditions	Reference
g-C₃N₄@ZIF-8	Rhombic dodecahedron	TC ¹ , RhB ² & Cr (VI) ³	TC (87.6%), Rh B (99.3%) & Cr (VI) (96.6%) in 60 min under the full spectrum irradiation	(Yuan et al. 2021)
ZnCDs/ZnO@ZIF-8	Polyhedrons	TC ¹	85% in 200 min under visible-light illumination	(Cheng et al. 2021)
Pt doped TiO₂- ZnO@ZIF-8	Polyhedral nano structure	Phenol	86.9% in 24h under UV light irradiation	(Jing et al. 2022)
ZIF-8-derived ZnO@In₂O₃	Hollow microtubes	TC ¹ , MG ⁴ , MB ⁵ & RhB ²	TC (93.2%), MG (80.6%), MB (25.9%) and RhB (8.6%) in 200 min under AM 1.5G sunlight simulator	(Li et al. 2021)

MoS₂-ZIF-8	Petal nanosheets	CIP ⁶ & TC ¹	CIP (93.2% in 180 min) & TC (75.6% in 180 min) -visible light irradiation	(Chen et al. 2019)
Porous ZIF-8	-	MeB ⁷ & Flu ⁸	MeB (99%) & Flu (25%) in 250 min under 450 W medium pressure mercury vapor lamp	(Soliman et al. 2022)
Ag/AgCl@ZIF-8 modified g-C₃N₄	Rhombic dodecahedron	Levofloxacin	87.3% in 60 min-visible light irradiations	(Zhou et al. 2019)
CdS/MOF-derived porous carbon	Polyhedral crystals	Cephalexin	93.1% in 50 min-300W Xe lamp	(Yang et al. 2017)
ZIF-8@PTA@AuNP	Rhombic dodecahedron	TC ¹	~86%-UV light exposure	(Beni et al. 2020)
Carbon nitride/porous zeolite	Globular tablet like	RhB ² , SuB ⁹ , TC ¹ and CIP ⁶	98% (RhB), 96% (SuB), 95% (TC), and 92% (CIP)- light irradiation	(Kumar et al. 2018)
MPg-C₃N₄-ZIF8	Spherical	TC ¹	74.8% in 180 min-visible light irradiations	(Li et al. 2019a)
C₃N₄-ZIF8		TC ¹	96% in 60 min-sunlight	(Panneri et al. 2017)
C-ZnS/ZnMoO₄ and C-ZnS/MoS₂ using ZIF8	Sphere like	TC ¹ & RhB ²	100% of TCH in 80 min and 100% of RhB in 120 min-300 W Xenon lamp	(Cui et al. 2019)

ZIF-8	Nanoparticles	MB ⁵	82.3%-visible light irradiation	(Jing et al. 2014)
MoSe₂	Nanoflower	RhB ²	99% within 5 mins-visible light irradiation	(Jiang et al. 2017)
MoSe₂-PANI	Nanosheets	RhB ² & CR ¹⁰	99.1% CR in 120 min and 83.2% RhB in 150 min- xenon arc lamp	(Mittal et al. 2019)
MoSe₂-PPy	Nanoparticles	RhB ² & CR ¹⁰	98.6% CR in 15 min and 84.4% RhB in 15 min- xenon arc lamp	(Mittal & Khanuja 2021)
TiO₂@ZIF-8	Spherical	MB ⁵	99.1%- UV light irradiation for 180 min	(Fu & Ren 2020)
TiO₂ NPs-ZIF8	Hexagonal	MB ⁵ & RhB ²	93% of MB and 57% of RhB in 120 min- UV-Visible light irradiation	(Chandra & Nath 2017)
BiMoO₆-ZIF8	Flower like structure	MB ⁵	66.88% in 100 min- 300W Xe lamp with 420nm cut-off filters	(Xia et al. 2019)
MoSe₂@ZIF-8	Rhombic dodecahedron	TC ¹ , MNZ ¹¹ & MG ⁴	~100% of TC, MNZ in 120 min and 98.6% of MG in 60 min- Xenon arc lamp	Present Study

294 ¹Tetracycline, ²Rhodamine B, ³Chromium Hexavalent, ⁴Malachite green, ⁵Methylene Blue, ⁶Ciprofloxacin, ⁷Methyl
 295 Blue, ⁸fluorescein, ⁹Sulforhodamine B, ¹⁰Congo Red, ¹¹Metronidazole

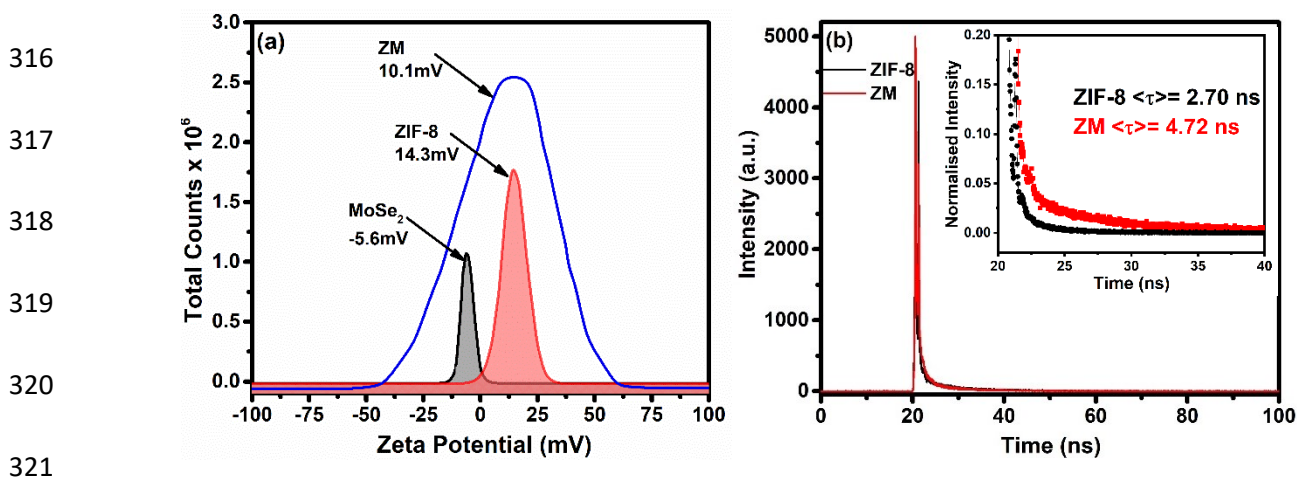
296 3.3.3. Surface charge

297 The surface charge of the photocatalyst plays an important role in the adsorption of the pollutant
 298 onto its surface. As observed in Fig. 7(a), the surface charge of MoSe₂, ZIF-8 and ZM
 299 nanocomposite are found to be -5.6, 14.3 and 10.1 mV, respectively. The surface charge of TC at
 300 4 < pH < 7 is positive whereas at 9 < pH < 12 the surface charge is negative (Li et al. 2019a). The
 301 surface charge of MNZ is neutral in the range of 4 < pH < 10 so it is not affected by the pH

302 conditions (Carrales-Alvarado et al. 2014). As observed in Fig. 6(f), ZM has high photocatalytic
 303 degradation efficiency for TC at pH 9 because of the competitive electrostatic attraction between
 304 the active species of TC (TC^{2-}) and the positive surface of ZM nanocomposite. However, when
 305 pH is 4 or 7, the dominant species of TC are TCH_2 and TCH^- and the adsorption capacity of ZM
 306 decreases because of the electrostatic repulsion (Li et al. 2019a). The higher degradation efficiency
 307 at basic conditions is in agreement with the zeta potential results.

308 3.3.4 Photogenerated charge carrier lifetime study

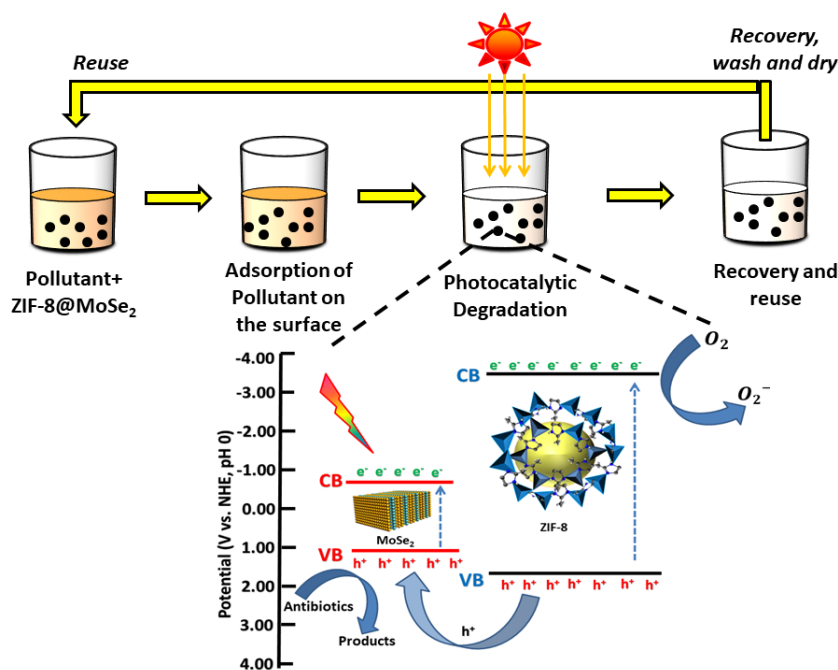
309 The photogenerated charge carrier dynamics have been studied with time correlated single- photon
 310 counting system (TCSPC) for ZIF-8 and ZM nanocomposite and the decay spectra are fitted with
 311 exponential function as shown in Fig. 7(b)(Mittal &Khanuja 2020b). The magnified portion of the
 312 spectra is as shown in the inset of Fig. 7(b). The average lifetime of photogenerated charge carriers
 313 in ZIF-8 and ZM nanocomposite were obtained to be 2.70 ns and 4.72 ns, respectively. The TCSPC
 314 results confirm that the construction of ZM nanocomposite is advantageous for efficient charge-
 315 carrier separation, which results in high photocatalytic activity for nanocomposite.



322 **Fig. 7: (a) Zeta Potential of MoSe₂, ZIF-8 and ZM nanocomposite and (b) TCSPC spectra of**
 323 **ZIF-8 and ZM nanocomposite upon excitation at 375 nm and emission at 425 nm, (inset)**
 324 **magnified image of TCSPC spectra**

325 3.4. Photocatalysis mechanism

326 The photocatalytic degradation mechanism of ZM nanocomposite was proposed and the schematic
 327 is as shown in Fig. 8. The heterojunction created by ZIF-8 and MoSe₂ is advantageous in enhancing
 328 photocatalytic activity by improving the photogenerated charge carrier generation, transfer and
 329 separation. The MoSe₂ and ZIF-8 could be excited by the light irradiation of energy larger than
 330 that of their forbidden band and photoinduced electrons transferred from valence band to
 331 conduction band in both ZIF-8 and MoSe₂. The photoinduced holes can be transferred from the
 332 VB of ZIF-8 (1.68 V) to VB of MoSe₂ (1.2 V), which helps in reducing the recombination rate
 333 (Mittal &Khanuja 2021, Wang et al. 2020b). However, due to the CB position of ZIF-8 (-3.41 V),
 334 the photogenerated electrons cannot move to the CB of MoSe₂ (-0.21 V) (Mittal &Khanuja 2021,
 335 Wang et al. 2020b). The electrons in CB can react with the dissolved O₂ to generate superoxide
 336 radicals ($O_2^{\bullet-}$) and holes in the VB react with water to form hydroxyl radicals (OH[•]). These radicals
 337 can react with the adsorbed pollutant and decompose it into simple and non-toxic molecules.

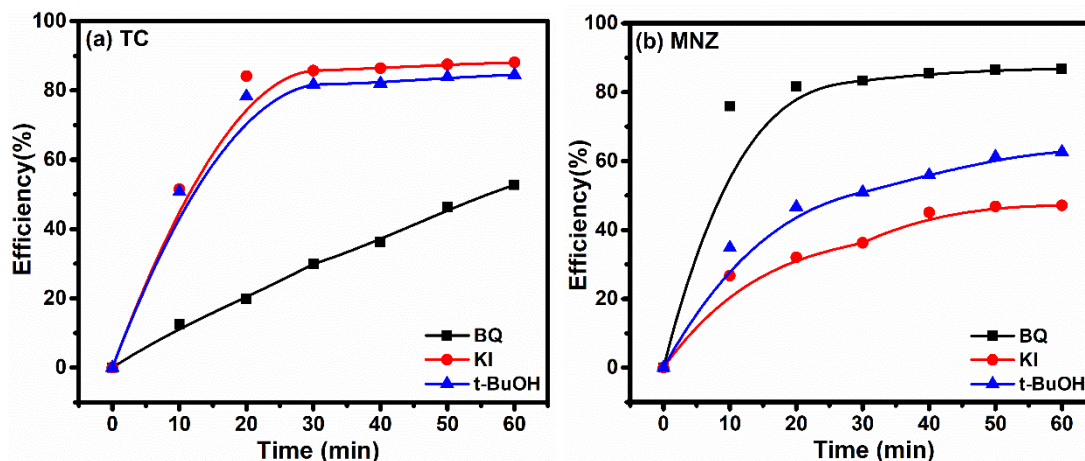


338 **Fig. 8: Schematic illustration of photocatalytic mechanism, reusability and charge transfer**
 339 **in the ZM nanocomposite under visible light irradiation**

340 3.4.1. Scavenger Test

341 To investigate the generation of active species and their role in the photocatalytic degradation
 342 process, tetra-butyl alcohol (t-BuOH), potassium iodide (KI) and para-benzoquinone (BQ) were
 343 used as OH[•], OH[•] & h⁺, and O₂^{•-} quenchers, respectively (Mittal &Khanuja 2020c). The

344 photocatalysis was performed in the presence of 20 mg of ZM nanocomposite in 100 mL of each
 345 TC and MNZ solution (1 mg/100 mL) and 1 mM of each scavenger under light irradiation for 60
 346 min and efficiency results are shown in the Fig. 9(a) and 9(b), respectively. The photodegradation
 347 efficiency of ZM for TC and MNZ was ~100 % without any scavenger in the solution and the
 348 photocatalytic degradation performance was significantly reduced with the addition of quenchers,
 349 and the degradation efficiency for TC was 52.7% with addition of BQ, 84.5% with t-BuOH and
 350 88.1% when KI was added. It can be concluded that the superoxide radicals are the main free
 351 radicals that are responsible for the degradation of TC (Qiang et al. 2019). In the scavenger test
 352 for the degradation of MNZ, the final degradation rate was 42.1% with addition of KI, 62.6% with
 353 t-BuOH and 86.7% when BQ was added. It can be concluded that the holes and hydroxyl radicals
 354 are mainly responsible for the degradation of MNZ (Ahmaruzzaman et al. 2019).

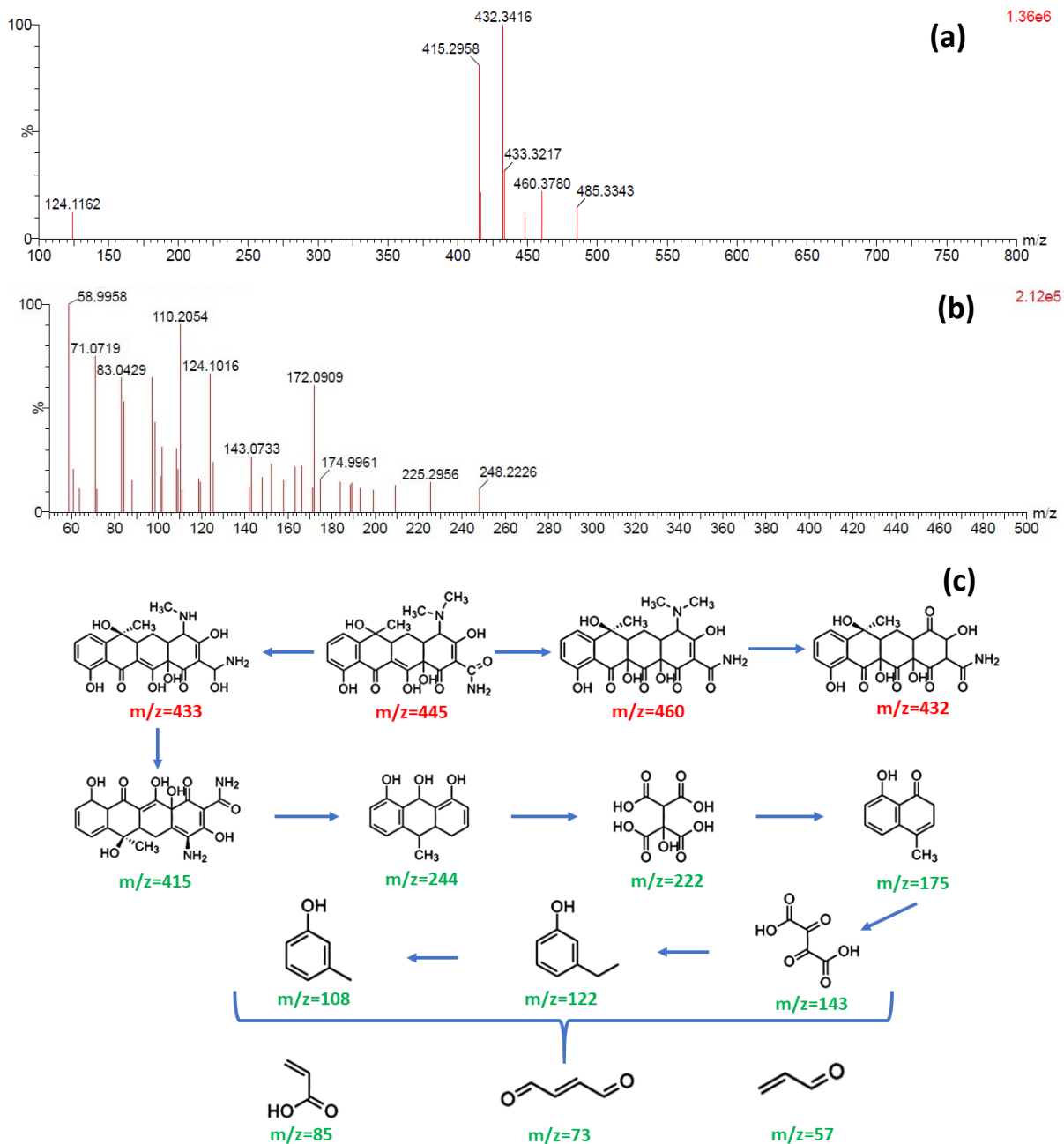


355 **Fig. 9: Photocatalytic degradation efficiency of ZM nanocomposite in the presence of para-**
 356 **benzoquinone (BQ), potassium iodide (KI) and tert-butyl alcohol (t-BuOH) for (a) TC and**
 357 **(b) MNZ**

358 3.4.2. Possible Photocatalytic Degradation Pathway of TC by LC-MS

359 The intermediate products generated during photocatalytic degradation of TC were investigated
 360 by LC-MS using the solution which were collected during photocatalytic reaction at 10 min and
 361 120 min. Fig. 10(a and b) shows the chromatographs at 10 and 120 min, respectively. The
 362 chromatograph in Fig. 10(a) shows that the TC ($m/z = 445$) degraded into the product with m/z
 363 value of 460 due to the hydroxylation of aromatic ring((Jeong et al. 2010)) (Li et al. 2019c, Luo et
 364 al. 2020). Further the simultaneously demethylation and oxidation of the TC resulted in the

365 formation of product with m/z value of 432 (Wang et al. 2018). The chromatograph shows that TC
366 was further oxidized by radicals, resulting in formation of ketone and a methyl group, forming a
367 new product after 120 min with m/z value of 433 and 415 (Zhang et al. 2020). The stepwise attack
368 of reactive oxygen species resulting in the simultaneously destruction of the 4-ring structure by
369 deamination and dihydroxylation resulting into products with m/z value of 244, 222 and 175. The
370 resulted product is further degraded into the product with m/z value of 143 via adding hydroxyl
371 groups, which in turn leads to the generation of product with m/z value of 122 via dihydroxylation
372 (Niu et al. 2013). The simpler ring-opened products, with m/z value of 85, 73 and 57 are the final
373 products formed after the photocatalytic degradation for 120 min (Li et al. 2019c). The degradation
374 pathway was proposed using these identified intermediate products and the structural identification
375 and m/z of these intermediate is shown in Fig. 10 (c). The intermediate products of m/z 460, 433
376 and 432 (labelled with red color in fig. 10(c)) are as toxic as TC but the finally degraded products
377 (labelled with green color in fig. 10(c)) are not harmful to the aquatic life (Wang et al. 2018). After
378 120 min of photocatalytic reaction, 99.4% of TC was degraded using ZM nanocomposite. Hence,
379 ZM nanocomposite exhibited a desirable degradation efficiency and a promising application
380 potential for antibiotics waste contaminated water treatment.



381
 382 **Fig. 10: LC-MS spectrum of degraded solution of TC at (a) 10 min, (b) 120 min and (c)**
 383 **possible photocatalytic degradation pathway for TC**

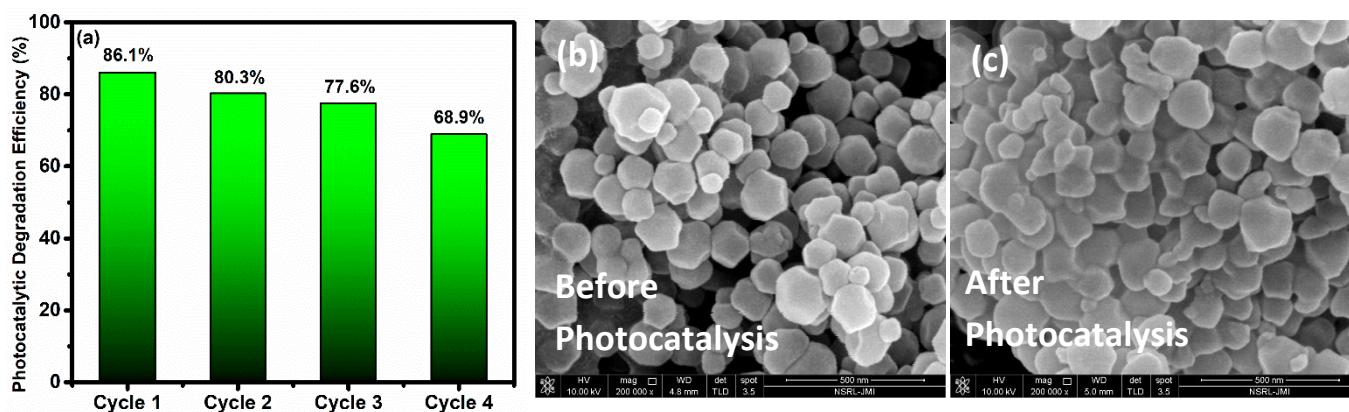
384 **3.5 Reusability of MoSe₂@ZIF-8 Nanocomposite**

385 To determine the reusability and regeneration ability of the ZM nanocomposite, four cycles of the
 386 photocatalytic degradation of TC were performed under light irradiation using 50 mg of ZM for

387 the degradation of TC with a concentration of 10 mgL⁻¹. After each cycle of the photocatalytic
 388 degradation, the ZM was extracted from the degradation solution by filtration and washed by milli
 389 Q water, followed by drying at 60 °C for 4 h. The ZM nanocomposite showed good photocatalytic
 390 degradation efficiencies, as shown in Fig. 11(a). The regeneration efficiency of the nanocomposite
 391 as calculated using eq. (iii) are 93.2%, 96.6% and 88.7% in 2, 3 and 4 cycles, respectively.

$$392 \text{ Regeneration efficiency (\%)} = \frac{\text{Degradation efficiency in } n\text{th cycle}}{\text{Degradation efficiency in } (n-1)\text{th cycle}} \times 100 \quad (\text{iii})$$

393 Moreover, the FESEM images of the as-prepared ZM nanocomposite and after 4 cycles of
 394 photocatalytic degradation are shown in Fig. 11(b and c). There is no visible change in the
 395 morphology of the catalyst. This indicates that ZM nanocomposite is a suitable and potential
 396 candidate for practical applications as a photocatalyst.



397
 398 **Fig. 11: Reusability and Regeneration of the ZM nanocomposite: (a) 4 cycles of the**
 399 **photocatalytic degradation of TC; FESEM image of the ZM nanocomposite (b) Before**
 400 **photocatalysis and (c) after 4 cycles of photocatalysis**

401 4.0. Conclusion

402 This study provided a cost-effective and potential photocatalytic material, which has the capability
 403 to treat water contaminated with antibiotics waste used for COVID-19. The superior degradation
 404 efficiencies were achieved for Tetracycline Hydrochloride, Metronidazole antibiotics and
 405 Malachite Green dye. As observed from the results the photocatalytic degradation efficiency of
 406 ZM nanocomposite was enhanced as compared to pristine MoSe₂ and ZIF-8 and the enhancement

407 could be attributed to the competitive absorption on the surface (as described through zeta
408 potential) of nanocomposite as well as improved photogenerated charge transfer and separation
409 efficiency (as explained through TCSPC results) resulting from the heterojunction between ZIF-8
410 and MoSe₂. The pH = 9 is optimal from the degradation rate of Tetracycline Hydrochloride
411 antibiotic. In the photocatalytic degradation of antibiotics, the main active species for degrading
412 Tetracycline Hydrochloride is superoxide radicals, while the main active species for the
413 degradation of Metronidazole are holes and hydroxyl radicals. The finally degraded products of
414 the antibiotic (TC) were not harmful to the aquatic organisms (as confirmed through LC-MS). The
415 photocatalyst retained good regeneration ability after four consecutive cycles, thereby confirming
416 reusability and regeneration ability of the ZM nanocomposite.

417 **Statement and Declarations**

418 **Ethical Approval:** We consciously assure that the manuscript is our own original work, which
419 has not been previously published elsewhere.

420 **Consent to Participate:** All authors have been personally and actively involved in substantial
421 work leading to the paper, and will take public responsibility for its content.

422 **Consent to Publish:** We have seen a version of the manuscript to be submitted/published
423 (including any pictures) and we hereby give our consent for publication in the Environmental
424 Science and Pollution Research.

425 **Author Contribution:** All authors contributed to the study conception and design. Material
426 preparation, data collection and analysis were performed by Honey Mittal, Aruna Ivaturi and
427 Manika Khanuja. All authors read and approved the final manuscript.

428 **Acknowledgement and Funding:** This work is financially supported by Department of Science
429 and Technology, India (DST/NM/NB/2018/203(G)(JMI)), Science and Engineering Research
430 Board, India (SERB, ECR/2017/001222) and Scottish Funding Council (SFC) Global Challenge
431 Research Fund (GCRF) David Livingstone Fellowship Project 2019-20. The authors also would
432 like to acknowledge the MRC, MNIT Jaipur and CIF, JMI, New Delhi.

433 **Competing Interest:** There are no Conflicts of interests.

434 **Availability of data and materials:** No datasets were generated or analyzed during the current
435 study

436 **References**

- 437 Adams C, Wang Y, Loftin K, Meyer M (2002): Removal of antibiotics from surface and distilled water in
438 conventional water treatment processes. *Journal of environmental engineering* 128, 253-260
- 439 Ahmaruzzaman M, Mohanta D, Nath A (2019): Environmentally benign fabrication of SnO₂-CNT
440 nano hybrids and their multifunctional efficiency as an adsorbent, catalyst and antimicrobial agent
441 for water decontamination. *Scientific reports* 9, 12935
- 442 Ashraf W, Bansal S, Singh V, Barman S, Khanuja M (2020): BiOCl/WS₂ hybrid nanosheet (2D/2D)
443 heterojunctions for visible-light-driven photocatalytic degradation of organic/inorganic water
444 pollutants. *RSC Advances* 10, 25073-25088
- 445 Barhoumi N, Oturan N, Ammar S, Gadri A, Oturan MA, Brillas E (2017): Enhanced degradation of the
446 antibiotic tetracycline by heterogeneous electro-Fenton with pyrite catalysis. *Environmental
447 Chemistry Letters* 15, 689-693
- 448 Beni FA, Gholami A, Ayati A, Shahrak MN, Sillanpää M (2020): UV-switchable phosphotungstic acid
449 sandwiched between ZIF-8 and Au nanoparticles to improve simultaneous adsorption and UV light
450 photocatalysis toward tetracycline degradation. *Microporous and Mesoporous Materials* 303,
451 110275
- 452 Bi E, Chen H, Yang X, Ye F, Yin M, Han L (2015): Fullerene-structured MoSe₂ hollow spheres anchored on
453 highly nitrogen-doped graphene as a conductive catalyst for photovoltaic applications. *Scientific
454 reports* 5, 13214
- 455 Carrales-Alvarado D, Ocampo-Pérez R, Leyva-Ramos R, Rivera-Utrilla J (2014): Removal of the antibiotic
456 metronidazole by adsorption on various carbon materials from aqueous phase. *Journal of colloid
457 and interface science* 436, 276-285
- 458 Chandra R, Nath M (2017): Multi-Core-shell TiO₂NPs@ZIF-8 Composite for Enhanced Photocatalytic
459 Degradation and Adsorption of Methylene Blue and Rhodamine-B. *ChemistrySelect* 2, 7711-7722
- 460 Chen W-Q, Li L-Y, Li L, Qiu W-H, Tang L, Xu L, Xu K-J, Wu M-H (2019): MoS₂/ZIF-8 hybrid materials for
461 environmental catalysis: solar-driven antibiotic-degradation engineering. *Engineering* 5, 755-767
- 462 Chen Z, Guo J, Jiang Y, Shao Y (2021): High concentration and high dose of disinfectants and antibiotics
463 used during the COVID-19 pandemic threaten human health. *Environmental Sciences Europe*
464 33:11, 10.1186/s12302-021-00456-4
- 465 Cheng Y, Wang X, Mei Y, Wang D, Ji C (2021): ZnCDs/ZnO@ZIF-8 Zeolite Composites for the Photocatalytic
466 Degradation of Tetracycline. *Catalysts* 11, 934
- 467 Chin M, Cisneros C, Araiza SM, Vargas KM, Ishihara KM, Tian F (2018): Rhodamine B degradation by
468 nanosized zeolitic imidazolate framework-8 (ZIF-8). *RSC advances* 8, 26987-26997
- 469 Cui Y-W, Zhang H-H, Yu S-Y (2019): Constructing ZIF-8 derived C-ZnS/ZnMoO₄@MoS₂ and C-ZnS/MoS₂
470 nanocomposites using a simple one-pot strategy to enhance photocatalytic degradation activity.
471 *RSC Advances* 9, 35189-35196
- 472 Daghri R, Drogui P (2013): Tetracycline antibiotics in the environment: a review. *Environmental chemistry
473 letters* 11, 209-227
- 474 Dharmaraj S, Ashokkumar V, Pandiyan R, Munawaroh HSH, Chew KW, Chen W-H, Ngamcharussrivichai C
475 (2021): Pyrolysis: An effective technique for degradation of COVID-19 medical wastes.
476 *Chemosphere* 275, 130092
- 477 Fu N, Ren X-c (2020): Synthesis of Double-Shell Hollow TiO₂@ZIF-8 Nanoparticles With Enhanced
478 Photocatalytic Activities. *Frontiers in Chemistry* 8: 578847

- 479 Ge P, Hou H, Banks CE, Foster CW, Li S, Zhang Y, He J, Zhang C, Ji X (2018): Binding MoSe₂ with carbon
480 constrained in carbonous nanosphere towards high-capacity and ultrafast Li/Na-ion storage.
481 Energy Storage Materials 12, 310-323
- 482 Gharebaghi R, Heidary F, Moradi M, Parvizi M (2020): Metronidazole; a potential novel addition to the
483 COVID-19 treatment regimen. Archives of academic emergency medicine 8, e40
- 484 Gironi LC, Damiani G, Zavattaro E, Pacifico A, Santus P, Pigatto PDM, Cremona O, Savoia P (2020):
485 Tetracyclines in COVID-19 patients quarantined at home: Literature evidence supporting Real-
486 World Data from a Multicenter Observational Study Targeting Inflammatory & Infectious
487 Dermatoses. Dermatologic therapy 34, e14694
- 488 Harpeness R, Gedanken A, Weiss A, Slifkin M (2003): Microwave-assisted synthesis of nanosized MoSe₂.
489 Journal of Materials Chemistry 13, 2603-2606
- 490 Huang Q, Li B, Yang S, Ma P, Wang Z (2013): Preparation and cyclodextrin solubilization of the antibacterial
491 agent benzoyl metronidazole. The Scientific World Journal 2013, 306476
- 492 Jeong J, Song W, Cooper WJ, Jung J, Greaves J (2010): Degradation of tetracycline antibiotics: mechanisms
493 and kinetic studies for advanced oxidation/reduction processes. Chemosphere 78, 533-540
- 494 Jia G, Liu L, Zhang L, Zhang D, Wang Y, Cui X, Zheng W (2018): 1D alignment of ZnO@ZIF-8/67 nanorod
495 arrays for visible-light-driven photoelectrochemical water splitting. Applied Surface Science 448,
496 254-260
- 497 Jiang Q, Lu Y, Huang Z, Hu J (2017): Facile solvent-thermal synthesis of ultrathin MoSe₂ nanosheets for
498 hydrogen evolution and organic dyes adsorption. Applied Surface Science 402, 277-285
- 499 Jing H-P, Wang C-C, Zhang Y-W, Wang P, Li R (2014): Photocatalytic degradation of methylene blue in ZIF-
500 8. Rsc Advances 4, 54454-54462
- 501 Jing Y, Yin H, Li C, Chen J, Wu S, Liu H, Xie L, Lei Q, Sun M, Yu S (2022): Fabrication of Pt doped TiO₂-ZnO@
502 ZIF-8 core@shell photocatalyst with enhanced activity for phenol degradation. Environmental
503 Research 203, 111819
- 504 Kaur H, Mohanta GC, Gupta V, Kukkar D, Tyagi S (2017): Synthesis and characterization of ZIF-8
505 nanoparticles for controlled release of 6-mercaptopurine drug. Journal of Drug Delivery Science
506 and Technology 41, 106-112
- 507 Kumar A, Samanta S, Srivastava R (2018): Systematic investigation for the photocatalytic applications of
508 carbon nitride/porous zeolite heterojunction. ACS Omega 3, 17261-17275
- 509 Kumar A, Singh S, Khanuja M (2020): A comparative photocatalytic study of pure and acid-etched template
510 free graphitic C₃N₄ on different dyes: An investigation on the influence of surface modifications.
511 Materials Chemistry and Physics 243, 122402
- 512 Kumar A, Mittal H, Nagar R, Khanuja M (2022): The synergistic effect of acid-etched gC₃N₄ nanosheets and
513 polyaniline nanofibers for the adsorption and photocatalytic degradation of textile dyes: a study
514 of charge transfer mechanism and intermediate products. Materials Advances,
515 <https://doi.org/10.1039/D1MA01218E>
- 516 Li D, Liu H, Niu C, Yuan J, Xu F (2019a): Mpg-C₃N₄-ZIF-8 composites for the degradation of tetracycline
517 hydrochloride using visible light. Water Science and Technology 80, 2206-2217
- 518 Li J, Liu L, Liang Q, Zhou M, Yao C, Xu S, Li Z (2021): Core-shell ZIF-8@MIL-68 (In) derived ZnO nanoparticles-
519 embedded In₂O₃ hollow tubular with oxygen vacancy for photocatalytic degradation of antibiotic
520 pollutant. Journal of Hazardous Materials 414, 125395
- 521 Li N, Zhou L, Jin X, Owens G, Chen Z (2019b): Simultaneous removal of tetracycline and oxytetracycline
522 antibiotics from wastewater using a ZIF-8 metal organic-framework. Journal of hazardous
523 materials 366, 563-572
- 524 Li Y, Cai X, Chen S, Zhang H, Zhang KH, Hong J, Chen B, Kuo D-H, Wang W (2018): Highly dispersed metal
525 carbide on ZIF-derived pyridinic-N-doped carbon for CO₂ enrichment and selective hydrogenation.
526 ChemSusChem 11, 1040-1047

- 527 Li Z, Guo C, Lyu J, Hu Z, Ge M (2019c): Tetracycline degradation by persulfate activated with magnetic
528 Cu/CuFe₂O₄ composite: efficiency, stability, mechanism and degradation pathway. *Journal of*
529 *hazardous materials* 373, 85-96
- 530 Li Z, Sun Y, Yang Y, Han Y, Wang T, Chen J, Tsang DC (2020): Comparing biochar-and bentonite-supported
531 Fe-based catalysts for selective degradation of antibiotics: Mechanisms and pathway.
532 *Environmental research* 183, 109156
- 533 Liu Z, Zhang Y, Zhao H, Li N, Du Y (2017): Constructing monodispersed MoSe₂ anchored on graphene: a
534 superior nanomaterial for sodium storage. *Science China Materials* 60, 167-177
- 535 Luanwuthi S, Krittayavathananon A, Srimuk P, Sawangphruk M (2015): In situ synthesis of permselective
536 zeolitic imidazolate framework-8/graphene oxide composites: rotating disk electrode and
537 Langmuir adsorption isotherm. *RSC Advances* 5, 46617-46623
- 538 Luo T, Feng H, Tang L, Lu Y, Tang W, Chen S, Yu J, Xie Q, Ouyang X, Chen Z (2020): Efficient degradation of
539 tetracycline by heterogeneous electro-Fenton process using Cu-doped Fe@Fe₂O₃: Mechanism
540 and degradation pathway. *Chemical Engineering Journal* 382, 122970
- 541 Medidi S, Markapurapu S, Kotupalli MR, Chinnam RKR, Susarla VM, Gandham HB, Sanasi PD (2018): Visible
542 Light Photocatalytic Degradation of Methylene Blue and Malachite Green Dyes with CuWO₄-GO
543 Nano Composite. *Modern Research in Catalysis* 7, 17-34
- 544 Mittal H, Kumar A, Khanuja M (2019): In-situ oxidative polymerization of aniline on hydrothermally
545 synthesized MoSe₂ for enhanced photocatalytic degradation of organic dyes. *Journal of Saudi*
546 *Chemical Society* 23, 836-845
- 547 Mittal H, Khanuja M (2020a): Nanosheets-and nanourchins-like nanostructures of MoSe₂ for
548 photocatalytic water purification: Kinetics and reusability study. *Environmental Science and*
549 *Pollution Research* 27, 23477-23489
- 550 Mittal H, Khanuja M (2020b): Interfacial charge carrier dynamics of the MoSe₂-conducting polymer
551 (MoSe₂-PANI) heterojunction. *Materials Today: Proceedings* 28, 314-316
- 552 Mittal H, Khanuja M (2020c): Optimization of MoSe₂ nanostructure by surface modification using
553 conducting polymer for degradation of cationic and anionic dye: Photocatalysis mechanism,
554 reaction kinetics and intermediate product study. *Dyes and Pigments* 175, 108109
- 555 Mittal H, Khanuja M (2021): Hydrothermal in-situ synthesis of MoSe₂-polypyrrole nanocomposite for
556 efficient photocatalytic degradation of dyes under dark and visible light irradiation. *Separation*
557 *and Purification Technology* 254, 117508
- 558 Niu J, Ding S, Zhang L, Zhao J, Feng C (2013): Visible-light-mediated Sr-Bi₂O₃ photocatalysis of tetracycline:
559 kinetics, mechanisms and toxicity assessment. *Chemosphere* 93, 1-8,
560 10.1016/j.chemosphere.2013.04.043
- 561 Panneri S, Thomas M, Ganguly P, Nair BN, Mohamed AP, Warriar K, Hareesh U (2017): C₃N₄ anchored ZIF
562 8 composites: photo-regenerable, high capacity sorbents as adsorptive photocatalysts for the
563 effective removal of tetracycline from water. *Catalysis Science & Technology* 7, 2118-2128
- 564 Peng H-J, Zheng P-Q, Chao H-Y, Jiang L, Qiao Z-P (2020): CdSe/ZIF-8-x: synthesis and photocatalytic CO₂
565 reduction performance. *RSC Advances* 10, 551-555
- 566 Qiang N, Shi T, Liu T (2019): In-depth study of the key factors affecting the degradation of antibiotics by
567 carbon nitride and its modified photocatalytic materials, *IOP Conference Series: Earth and*
568 *Environmental Science*. IOP Publishing, pp. 032051
- 569 Qin K, Zhao Q, Yu H, Xia X, Li J, He S, Wei L, An T (2021): A review of bismuth-based photocatalysts for
570 antibiotic degradation: Insight into the photocatalytic degradation performance, pathways and
571 relevant mechanisms. *Environmental Research*, 111360
- 572 Qiu J, Zhang X, Feng Y, Zhang X, Wang H, Yao J (2018): Modified metal-organic frameworks as
573 photocatalysts. *Applied Catalysis B: Environmental* 231, 317-342

- 574 Saghi M, Mahanpoor K (2017): Photocatalytic degradation of tetracycline aqueous solutions by
575 nanospherical α -Fe₂O₃ supported on 12-tungstosilicic acid as catalyst: Using full factorial
576 experimental design. International Journal of Industrial Chemistry 8, 297-313
- 577 Shinde P, Sharma V, Punde A, Waghmare A, Vairale P, Hase Y, Pandharkar S, Bhorde A, Aher R, Nair S
578 (2021): 2D alignment of zinc oxide@ ZIF8 nanocrystals for photoelectrochemical water splitting.
579 New Journal of Chemistry 45, 3498-3507
- 580 Si Y-h, Li Y-y, Xia Y, Shang S-k, Xiong X-b, Zeng X-r, Zhou J (2018): Fabrication of novel ZIF-8@BiVO₄
581 composite with enhanced photocatalytic performance. Crystals 8, 432
- 582 Siddiqui I, Mittal H, Kohli VK, Gautam P, Ali M, Khanuja M (2018): Hydrothermally synthesized micron
583 sized, broom-shaped MoSe₂ nanostructures for superior photocatalytic water purification.
584 Materials Research Express 5, 125020
- 585 Sodhi M, Etmnan M (2020): Therapeutic Potential for Tetracyclines in the Treatment of COVID-19.
586 Pharmacotherapy: The Journal of Human Pharmacology and Drug Therapy 40, 487-488
- 587 Soliman AI, Abdel-Wahab A-MA, Abdelhamid HN (2022): Hierarchical porous zeolitic imidazolate
588 frameworks (ZIF-8) and ZnO@N-doped carbon for selective adsorption and photocatalytic
589 degradation of organic pollutants. RSC advances 12, 7075-7084
- 590 Stackelberg PE, Gibs J, Furlong ET, Meyer MT, Zaugg SD, Lippincott RL (2007): Efficiency of conventional
591 drinking-water-treatment processes in removal of pharmaceuticals and other organic
592 compounds. Science of the Total Environment 377, 255-272
- 593 Tsai W-T (2021): Analysis of medical waste management and impact analysis of COVID-19 on its
594 generation in Taiwan. Waste Management & Research 39, 27-33, 0734242X21996803
- 595 Ulu A (2020): Metal–organic frameworks (MOFs): a novel support platform for ASNase immobilization.
596 Journal of Materials Science 55, 6130-6144
- 597 Wang F, Zhang Y, Ming H, Wang L, Zhao Z, Wang Y, Liang J, Qin Y (2020a): Degradation of the ciprofloxacin
598 antibiotic by photo-Fenton reaction using a Nafion/iron membrane: role of hydroxyl radicals.
599 Environmental Chemistry Letters 18, 1745-1752
- 600 Wang J, Zhi D, Zhou H, He X, Zhang D (2018): Evaluating tetracycline degradation pathway and
601 intermediate toxicity during the electrochemical oxidation over a Ti/Ti₄O₇ anode. Water research
602 137, 324-334
- 603 Wang T, Wang Y, Sun M, Hanif A, Wu H, Gu Q, Ok YS, Tsang DC, Li J, Yu J (2020b): Thermally treated zeolitic
604 imidazolate framework-8 (ZIF-8) for visible light photocatalytic degradation of gaseous
605 formaldehyde. Chemical Science 11, 6670-6681
- 606 Wu C, Liu Q, Chen R, Liu J, Zhang H, Li R, Takahashi K, Liu P, Wang J (2017): Fabrication of ZIF-8@SiO₂
607 micro/nano hierarchical superhydrophobic surface on AZ31 magnesium alloy with impressive
608 corrosion resistance and abrasion resistance. ACS applied materials & interfaces 9, 11106-11115
- 609 Xia Y, Shang S-k, Zeng X-r, Zhou J, Li Y-y (2019): A novel Bi₂MoO₆/ZIF-8 composite for enhanced visible light
610 photocatalytic activity. Nanomaterials 9, 545
- 611 Yang C, Cheng J, Chen Y, Hu Y (2017): CdS nanoparticles immobilized on porous carbon polyhedrons
612 derived from a metal-organic framework with enhanced visible light photocatalytic activity for
613 antibiotic degradation. Applied Surface Science 420, 252-259
- 614 Yuan X, Qu S, Huang X, Xue X, Yuan C, Wang S, Wei L, Cai P (2021): Design of core-shelled g-C₃N₄@ZIF-8
615 photocatalyst with enhanced tetracycline adsorption for boosting photocatalytic degradation.
616 Chemical Engineering Journal 416, 129148
- 617 Zhang Q, Jiang L, Wang J, Zhu Y, Pu Y, Dai W (2020): Photocatalytic degradation of tetracycline antibiotics
618 using three-dimensional network structure perylene diimide supramolecular organic
619 photocatalyst under visible-light irradiation. Applied Catalysis B: Environmental 277, 119122

620 Zhou J, Liu W, Cai W (2019): The synergistic effect of Ag/AgCl@ZIF-8 modified g-C₃N₄ composite and
621 peroxydisulfate for the enhanced visible-light photocatalytic degradation of levofloxacin.
622 Science of The Total Environment 696, 133962

623

624